Stability and thermoelectric performance of doped Higher Manganese Silicide materials solidified by RGS (Ribbon Growth on Substrate) synthesis

Pierre-Yves Pichon*[a], Pierre Berneron[a], Joshua Levinsky[b], Arjan Burema[b], Graeme Blake[b], David Berthebaud[c], Stéphanie Gascoin[c], Franck Gascoin[c], Sylvie Hebert[c], Jonas Amtsfeld[d], Tijmen Hommels[d], Mark Huijben[d], Johannes de Boor[e], Eckhard Müller[e,g], Christelle Navone[f], Axel Schönecker[a]

*corresponding author: pichon@rgsdevelopment.nl

List of co-authors e-mail addresses (in order of appearance in the author list):
berneron@rgsdevelopment.nl; j.levinsky@rug.nl; a.a.burema@rug.nl; g.r.blake@rug.nl;
David.BERTHEBAUD@cnrs.fr; stephanie.gascoin@ensicaen.fr; franck.gascoin@ensicaen.fr;
sylvie.hebert@ensicaen.fr; jonas.amtsfeld@gmail.com; tijmenhommels@hotmail.com
m.huijben@utwente.nl; johannes.deboor@dlr.de; Eckhard.Mueller@dlr.de; christelle.navone@cea.fr;
schonecker@rgsdevelopment.nl

[a]RGS Development B.V., Bijlestaal 54a, 1721 PW Broek op Langedijk, Netherlands

[b]Zernike Institute for Advanced Materials, University of Groningen, Nijenborgh 4, 9747AG Groningen, Netherlands

[c]Normandie Univ, ENSICAEN, UNICAEN, CNRS, CRISMAT, UMR6508, 14000 Caen, France

[d]MESA+ Institute for Nanotechnology, University of Twente, 7500 AE Enschede, Netherlands

[e]German Aerospace Center, Institute of Materials Research, Linder Höhe, 51147 Köln, Germany

[f]CEA, LITEN, 17 rue des Martyrs, BP166, 38042 Grenoble, France

[g]Justus Liebig University Gießen, Institute of Inorganic and Analytical Chemistry, 35392 Gießen, Germany

Abstract

Large scale deployment of thermoelectric devices requires that the thermoelectric materials have stable electrical, thermal and mechanical properties under the conditions of operation. In this study we examine the high temperature stability of higher manganese silicide (HMS) materials prepared by the RGS (ribbon growth on substrate) technique. In particular we characterize the effect of element substitution on the structural and electrical changes occurring at the hot side of temperatures of thermoelectric devices relevant to this material (600°C). Only by using suitable substitution (4% vanadium at the Mn site) can we obtain temperature-independent structural parameters in the range 20°C - 600°C, a condition that results in stable electrical properties. Additionally, we show that 4% vanadium substitution at the Mn site offers the best thermoelectric figure of merit among the different compositions reported here with ZT_{max}=0.52, a value comparable to the state of the art for HMS materials. Our analysis suggests that ionized impurity scattering is responsible for the better performance of this material.

1 Introduction

The higher manganese silicide (HMS, MnSi$_\gamma$) phases are the most silicon-rich materials of the Mn-Si alloys. Among the different classes of thermoelectric materials relevant to thermoelectric power generation applications (e.g. PbTe-based alloys [1–3], half-Heusler [4]), HMS materials are promising candidates for the deployment of large scale, cost-effective thermoelectric generators operating up to 600°C thanks to their low raw material cost and good thermoelectric performance. The thermoelectric figure of merit (*ZT*) characterizes the effectiveness of a material to transform a heat flow into electrical power. It is defined as $ZT = S^2\sigma T/\kappa$, where *S* is the Seebeck coefficient, σ is the electrical conductivity, κ is the thermal conductivity, and *T* is the absolute temperature. Competitive *ZT* values in the range 0.5-0.7 have been measured on doped HMS materials synthesized by different techniques, which makes them technologically relevant for integration into thermoelectric devices[5–8], possibly in combination with n-type silicides (SiGe alloys, Mg$_2$(Si,Ge,Sn)[9,10]). Recently, supersaturated HMS materials synthesized by melt spinning achieved significantly improved performance with *ZT* values of about 1 for p-type Re-doped HMS [11–13]. Until now most of the work on thermoelectric materials has focused on increasing *ZT*. However, an important condition for successful large-scale deployment of high temperature thermoelectric devices is the stability of the thermoelectric properties at the relevant temperature and atmospheric conditions. The first objective of this work is to systematically characterize the high temperature electrical stability of HMS materials produced by the Ribbon Growth on Substrate (RGS) production process. We aim at clarifying the relations between electrical stability, doping type and structural evolution under high temperature module operation conditions. In this article we also demonstrate a significant improvement of both electrical stability and *ZT* for vanadium-doped HMS associated with ionized impurity scattering of the charge carriers and subsequent superior electrical and thermal properties.

The HMS phases belong to the family of so-called chimney-ladder structures: a [Mn] 'chimney' subsystem and a [Si] 'ladder' subsystem having a common *a*-axis but different stacking periods in the *c* direction, hence different subsystem *c*-axis lengths c_{Mn} and c_{Si}. Examination of the crystal structure shows that $\gamma = c_{Mn}/c_{Si}$. If γ is an irrational number the structure is incommensurate and cannot be described using a single overall lattice parameter in the *c* direction: this motivates the structural characterization of HMS in terms of two separate subsystems or by the (3+1) dimensional superspace approach[14]. More recently another approach was proposed to model the XRD spectrum of the HMS structure by including significant defects in the Si sublattice [15]. The valence electron count (*VEC*) concept is useful to describe the thermodynamic stability of chimney-ladder phases and to estimate the charge carrier density of these materials from the structural parameter γ [16–19]. The *VEC* is the number of valence electrons per transition metal element (here Mn). For unsubstituted MnSi$_\gamma$, $VEC = 7 + 4\gamma$. For the general case of substituted HMS it can be written as:

$$VEC = 7(1 - x) + V_{Me}\, x + (4(1 - y) + V_S\, y)\gamma \qquad (1)$$

Here *x* and V_{Me} are the proportion and number of valence electrons of the element *Me* that substitutes Mn (e.g., $V_V = 5$); *y* and V_s are the proportion and number of valence electrons of the element that substitutes Si (e.g., $V_{Al} = 3$; $V_{Ge} = 4$). Furthermore, the charge carrier density can be estimated by:

$$[p] = \frac{4(14 - VEC)}{\mathcal{V}} \qquad (2)$$

In equation (2) $\mathcal{V}$ is the volume of the Mn subcell. Here we consider only the case where *VEC*<14 (p-type materials). In general, chimney-ladder phases are stabilized for a *VEC* count of 14 [16,17]. Therefore, according to equation (2) stable chimney ladder phases should be charge neutral: in fact thermodynamic stability relates to the opening of a bandgap around the chemical potential. For the HMS phase the stoichiometry Mn$_4$Si$_7$ ($\gamma = 1.75$) should be preferred, however structural analysis has shown that compounds with lower γ are actually synthesized , conferring to this material an intrinsic p-

type character. Kawasumi *et al.* identified $Mn_{15}Si_{26}$ as the stoichiometry of undoped-HMS solidified by the Bridgman method[20] and also measured a hole density of about 2×10^{27} m^{-3} in the room temperature-to 600 K range [20], as predicted by equation (2) (*[p]*=1.98 × 10^{27} m^{-3}). Early works identified $Mn_{15}Si_{26}$ ($\gamma = 1.733$), $Mn_{11}Si_{19}$ ($\gamma = 1.727$), and $Mn_{27}Si_{47}$ ($\gamma = 1.741$)) as commensurate structures[20–22], while more recent studies report intermediate γ values, interpreting these as either incommensurate, incorporating defects at the Si sites, or comprising domains of different γ values [14,15,23–25].

Several studies have shown that undoped HMS can undergo solid-solid phase transitions in the temperature range useful for thermoelectric generation. For example a comparative study of Differential Thermal Analysis (DTA), Differential Scanning Calorimetry (DSC) and High Temperature powder X-Ray Diffraction (HTXRD) showed that solid-solid phase transformations occur upon heating[26]. These transitions are primarily due to a temperature-dependence of the γ ratio: another HTXRD study of undoped HMS showed that the expansion rates of the Si and Mn sublattices in the *c* direction are different upon heating. As a result γ increases and the structure expels Mn, resulting in MnSi precipitation in the form of layered precipitates parallel to the *a-b* crystallographic plane [18]. In this study the authors suggest that the long-term stability of the material may be compromised due to cracks occurring at the HMS-MnSi interface. Cracking issues in the *a-b* plane have been a general concern for HMS solidified from the liquid[27], the cause being the lattice mismatch between the HMS phase and the MnSi phase precipitated during cooling from the melting point[28,29]. Another group synthetized undoped MnSi-free single crystals by a chemical vapor transport and showed that MnSi precipitates appeared upon heating at about 900°C, resulting from the thermodynamically stable γ being temperature-dependent **[30]**. Finally, another HTXRD study showed that the addition of alloying elements at the Mn or Si site can significantly influence the relative expansion coefficient of the sublattices, i.e. the *$\gamma(T)$* characteristic. For example, in the case of Ge doping γ is stable between room temperature and 600 °C[24]. This suggests that appropriate doping may stabilize the HMS phase in the temperature range of interest. Notably, above a critical Ge concentration the layered MnSi precipitates disappeared in crystals grown by the Czochralski technique[27].Despite several literature reports on the HMS phases show the occurrence of a solid-solid reactions in the temperature range of interest for thermoelectric applications, very little information is available on the stability of the thermoelectric properties, and on their relations with the synthesis technique, the concentration of a particular substitution element, and the corresponding *$\gamma(T)$* characteristics. Most papers have reported the thermoelectric properties of as-synthesized materials, without demonstrating that the materials are thermodynamically and/or electrically stable. The motivation of this work is to bridge the gap between stability studies and performance studies of the HMS materials. In this framework, here we examine the effects of doping on the (micro)structural evolution of HMS and on the changes in thermoelectric properties at high temperatures. We study the effect on the thermoelectric properties of maintaining the materials at a temperature of 600°C in ambient atmosphere. Based on a review of the literature, we expected that synthesis techniques involving relatively fast cooling such as RGS (about 2 K/sec above 500 °C) may result in metastable γ after synthesis. Upon further high temperature exposure in devices this might result in MnSi precipitation, cracking, and changes in *[p]*. Therefore, we use HTXRD to characterize *$\gamma(T)$* in the room temperature-to 600°C range and to explain changes in the microstructure, in the charge carrier density and in the mobility upon aging. This work is reported in section 3.1.

At this point it is necessary to clarify how we define 'stability' throughout this paper. We choose a practical definition from the point of view of the application (use of HMS as an active material in thermoelectric generators) and focus on achieving stable thermoelectric properties. The material has to serve for a designed operation time at specified temperature and atmosphere conditions (here 600°C in air) and shall not decay more than a few percent in performance over this time. With the relatively high crystallization velocities achieved in the RGS process we cannot synthetize thermodynamically stabilized crystals (i.e. electrically and chemically homogeneous and monocrystalline) and as such we do not aim at studying the properties of a thermodynamically stabilized HMS crystal. Strictly speaking thermodynamic stability implies that the material is in

thermal equilibrium with its environment, and this will never be the case in a thermoelectric device where a thermal gradient is applied. Additionally under such a thermal gradient if γ is temperature-dependent the material structure will be different at the hot and the cold side. Besdies some level of inhomogeneity is very often reported in HMS, whether it is present at the structural level [15,22], or at the scale of the microstructure (segregation during growth, precipitates, grain boundaries) [23]. In fact many good thermoelectric materials could be described as thermodynamically unstable as it is common to purposely introduce disorder, some complexity in the microstructures or precipitates of second phases to optimize their thermoelectric properties. A major challenge in developing such material for practical application is therefore to stabilize the defects at temperatures and timescales of the application environment.

Since the doping type and level are key parameters affecting the $\gamma(T)$ characteristics, we chose a set of nominal compositions based on promising materials reported so far. $Mn[Si_{0.9955}Al_{0.0045}]_{1.73}$ was chosen because of the good thermoelectric properties already reported[5]. We selected $Mn[Si_{0.991}Ge_{0.009}]_{1.73}$ because of the reported effects of Ge on $\gamma(T)$ and MnSi precipitation [27,31,32]. Mn substitution by Re was also chosen because it yields a state of the art ZT value [11], but we opted for a lower doping amount of $[Mn_{0.97}Re_{0.03}]Si_{1.73}$ to avoid Re silicide formation during synthesis with our RGS technique. The substitution of V for Mn above 2% was recently shown to suppress the formation of MnSi precipitates while highly disordered strained Si domains appeared instead [33,34]. Therefore, we included $[Mn_{0.98}V_{0.02}]Si_{1.73}$ and $[Mn_{0.96}V_{0.04}]Si_{1.73}$ as nominal compositions. Throughout the following discussion the materials will be referred to by the percentage of substituted elements, such as '4%V-HMS' for $[Mn_{0.96}V_{0.04}]Si_{1.73}$. While characterising these materials we noticed that V-doped materials exhibit significantly different electrical properties compared to the others. A comparative analysis of the thermoelectric performance of the different materials is the subject of section 3.2.

2 Materials and methods

2.1 Synthesis

The materials were synthesized by solidification from the melt using the RGS process. This solidification technique consists in moving a flat mould band (kept at a temperature several hundred Celsius lower than the melting point) under the liquid melt, which is contained in a continuously refilled reservoir. The liquid is solidified at a growth rate between 0.1 and 1 $mm.s^{-1}$ resulting in a sheet of typical thickness 0.5 mm grown on the mould. The solidified semiconductor sheet detaches upon cooling, can be transferred out of the process chamber and the mould can be reused. A detailed description of the process is given in [35,36]. The solidification velocity is intermediate between that of large batch growth processes (the Czochralski, floating zone, directional solidification and Bridgman techniques have a solidification velocity of about 10^{-5}-10^{-4} $m.s^{-1}$) and non-equilibrium processes such as spin casting with a solidification velocity of several $m.s^{-1}$. Therefore, RGS materials have unique (micro)structures and electrical properties. This process is interesting from a technological point of view as it allows for HMS thermoelectric legs of controlled dimensions to be produced in one step and at rates compatible with the large-scale deployment of thermoelectric generators.

2.2 Characterization

The stability of the materials was tested under two types of conditions. In a first series of tests the Seebeck coefficient and the electrical conductivity of as-solidified samples were measured as a function of time at 600 °C in inert gas (12 to 45 hours). Such measurements were done routinely at University of Groningen and selected samples were measured at CEA and University of Twente for confirmation. In a second series of tests the samples were subjected to annealing steps at 600 °C for 10 hours, then for 100 hours in air. These testing conditions are more relevant to practical applications since a thermoelectric material that is usable in oxidative environments opens the door to more cost-effective module designs compared to, e.g. encapsulated module configurations. The Seebeck

coefficient and electrical conductivity were measured at room temperature on each sample in the as-grown state, after 10 hours of annealing and after 10+100 hours of annealing. Additional samples were undergoing the same annealing sequence and were analysed by Hall measurements, microstructure analysis, HTXRD and thermoelectric performance evaluation. For all samples where the Seebeck coefficient and/or electrical conductivity were measured (including Hall samples), one surface of the RGS-cast HMS sheet samples was ground to reduce thickness inhomogeneities.

Note that our analysis plan allowed for cross-checking of the measurements performed at three different laboratories for the room temperature Seebeck coefficient and at four different laboratories for the electrical conductivity. We verified *a posteriori* that the error bars indeed overlap.

2.2.1 Stability: structure and microstructure

Samples on which the microstructure was studied were embedded in epoxy resin and polished (last step using a 1μm diamond suspension) for analysis by optical microscopy and Scanning Electron Microscopy (SEM). In order to reveal the presence of MnSi precipitates the polished cross-sections were submitted to a dilute HF etching step (HF:H2O=5:95, typically 10 s). SEM analysis was performed using a Hitachi SU70 electron microscope with an acceleration voltage of 15kV and a working distance of 15mm. Energy dispersive X-ray spectroscopy (EDX) was carried out on some samples to identify the different phases present and evaluate the composition homogeneity.

High resolution powder or bulk surface X-ray diffraction data were collected using a Bruker D8 Advance Vario 1 two-circle diffractometer (θ-2θ Bragg-Brentano mode) using Cu Kα radiation (λ=1.540598 Å) with a Ge (1 1 1) monochromator (Johansson type) and a Lynx Eye detector. High-temperature experiments were carried out with an Anton Paar furnace HTK1200N; the temperature was regulated within ±3 K. Data were collected over the angular range $10 \leq 2\theta$ (°) ≤ 95 under air, measuring for 1 s at each angular increment of 0.0157° (1.5 h /scan). XRD patterns were recorded using the following temperature profile: a pattern at room temperature; one every 100 K from 373 K to 873 K (heating rate of 30 K/min); one every 100 K from 873 K to 373 K (cooling rate of 30 K/min); one at room temperature after cooling. The Le Bail method was employed to refine the lattice parameters and modulation vectors. Refinements were performed in the (3 + 1)-dimensional superspace group I41/amd(00g)00ss using the JANA2006 software package[37].

2.2.2 Stability: thermoelectric properties

The Seebeck coefficient and electrical conductivity were measured simultaneously using a Linseis LSR-3 apparatus at the University of Groningen. To measure the Seebeck coefficient a temperature gradient of 30 K was applied across the sample and the induced voltage was measured at a constant current. The resistivity was measured using a four-point probe configuration where all contact points are aligned along a vertical line. To characterize the evolution of the electrical resistivity and Seebeck coefficient at elevated temperature, the samples were held at 600 ˚C for 14 hours under a protective helium atmosphere to prevent oxidation.

For the samples annealed in air at 600 ˚C the Seebeck coefficient and electrical conductivity were measured at room temperature on a custom-made test bench at RGS Development B.V. An HF dip was performed before the measurement to remove the oxide layer grown during the annealing step. The electrical conductivity was measured on a four-point probe system using an electrical current of 0.5 A over the (measured) sample cross-section area of approximately 0.4 x 15 mm^2. The error of the electrical conductivity is estimated to be less than 8%, the highest error contribution coming from thickness variations. The Seebeck coefficient was evaluated by measuring the voltage drop generated by a temperature difference of 8 K around room temperature. The temperature difference was applied using commercially available Peltier elements and measured using type T thermocouples.

To evaluate the change in charge carrier density and mobility upon annealing, Hall measurements were carried out at CRISMAT labs on as-solidified samples and samples annealed for 10 hours at 600 ˚C in air. The measurements were performed in a PPMS system from Quantum Design, where the electrical contacts were soldered with indium on samples with a shape 5 × 5 × 0.4

mm. The carrier density was extracted from Hall effect measurements from 5 K to 300 K considering as a first approximation a simple single band model, to compare with the results from the literature [5,34]. Electrical resistivity was measured using the van der Pauw geometry. Note that the measurements were performed in plane, and no noticeable anisotropy was detected during the Van der Pauw experiments. This is consistent with EBSD analysis which showed that the out of plane direction corresponds to the c axis direction. From both sets of measurements, the mobility could be extracted. For the resistivity the main source of error comes from the thickness determination, with a maximal error of ~ 8% except for the V-doped materials where the error is ~ 12% due to thinner solidified samples, and from the contact size and misalignment, estimated to be ~ 5%. The intrinsically high charge carrier density of HMS materials makes the measurement accuracy particularly sensitive to errors in the measurement of the slope of the Hall resistance curves R(H). All the carrier concentrations determined here are extracted from linear R(H) curves, the uncertainty in the linear least squares fit being less than 0.5%.

2.2.2 Thermoelectric performance

Samples were measured at DLR to evaluate their thermoelectric performance. The samples were polished before the measurements to decrease the surface roughness and improve the electrical contacts. The electrical conductivity σ and the Seebeck coefficient S of the samples were measured concurrently using a custom-built setup. Setup details and a detailed description of the data analysis for the Seebeck coefficient measurements can be found in published works[38,39]. Due to the small thickness and the sometimes uneven surface, the uncertainty for the electrical conductivity is estimated to be 10%, while the uncertainty for the Seebeck coefficient is 5%. The measurement data were acquired both during heating up and during cooling down. The thermal diffusivity (α) of the samples was obtained using a Netzsch LFA 467HT apparatus. The density ρ was determined using Archimedes' method, while the heat capacity C_P was measured using a Netzsch DSC 404. The thermal conductivity (κ) was obtained using the relation $\kappa = \alpha\rho C_P$ and the measurement accuracy is estimated to be 10 %, the uncertainty stemming mainly from the C_P measurement and the thickness sensitivity of the LFA measurement. Note that for practical reasons of sample geometry the conductivity (and Seebeck coefficient) are determined in-plane, while thermal conductivity is determined cross-plane. Therefore the ZT results reported here should be seen as best estimates, since one cannot exclude possible anisotropic effects.

3 Results and Discussion

3.1 Stability

3.1.1 Stability of the electrical properties

Figure1 shows measurements of the Seebeck coefficient and electrical conductivity as a function of time at 600˚C for 4%V-HMS, 0.9%Ge-HMS, 0.45%Al-HMS, and 3%Re-HMS. The measurements show that the electrical resistivity increases by between 6% and 20% during the 12 h of measurement time for the Ge, Al and Re doped samples. Note that for these samples the electrical resistivity still continues to increase at the end of the test. In contrast, the electrical resistivity of 4%V-HMS is found stable over time and does not vary within the measurement error. Changes in the Seebeck coefficient, if any, are at most 2% based on data analysis after noise filtering, which is relatively small compared to changes in the resistivity. Our data show that the 4%V-HMS has stable electrical properties at 600˚C, a typical hot-side thermoelectric module temperature. We confirmed this observation by measuring additional samples at different laboratories for up to 45 hours. Figure S1 in the supplementary information shows the evolution of the electrical properties of 4%V-HMS and 0.45%Al-HMS as a function of time. Figure 2 summarizes these results by showing a comparison of the high temperature power factor of different materials as-solidified and after 10 hours exposure to 600˚C.

Since we are interested in the material stability under atmospheric conditions, we also measured the changes of the room temperature electrical conductivity and Seebeck coefficient for samples that had undergone successive annealing for 10 h and 100 h in air at 600 ˚C. The effect of the

two annealing steps on the room temperature electrical properties is shown in figure 3. Except for 4%V-HMS where the electrical properties do not change, the electrical conductivity of all materials (including 2%V-HMS) decreases by 20-25% after 10 + 100 hours of annealing, while the change in the Seebeck coefficient is relatively smaller. Figure 2 and figure 3 show that the decrease in electrical conductivity on annealing results in a significant reduction of the power factor $S^2\sigma$, with the exception of 4%V-HMS. Note that the material with the highest power factor before thermal treatment is the Ge-doped material but after annealing the V-doped materials have the best electrical properties. Additionally, we conclude that the testing atmosphere is likely not the most influential parameter to explain the changes in electrical properties, and that a minimum vanadium concentration is required to stabilize the electrical conductivity.

3.1.2 Structure and microstructure analysis

The purity of the 2%V-HMS, 4%V-HMS, and 0.45%Al-HMS materials and the absence of any significant volume fraction of secondary phases were checked by XRD measurements on powder samples derived from as-solidified materials. The XRD patterns are shown in figure 4 and demonstrate the absence of significant amounts of MnSi, Al-rich or V-rich phases. The variation of peak intensity is due to preferential orientation effects. All peaks could be indexed as HMS phase with superspace group I41/amd(00γ)00ss according to the composite structural model suggested by Miyazaki et al.[40]. According to research on the Mn-Si-Al system, excess Al-doping would result in the formation of Al-rich phases with about 30at% Al (C40 or C54 phase)[41,42], which are not observed in our case. This confirms that the chosen Al doping level is below the solubility limit as already demonstrated by Chen et al.[5]. Similarly, we do not observe any signal from VSi_2 in 2%V-HMS and 4%V-HMS, which would be the case if we significantly exceeded the solubility limit of V in the HMS phase. However, Miyazaki et al. suggested that the solubility limit of V substituting Mn in HMS is 3% [33]. As will be discussed later, small amounts of the MnSi phase are present in all materials but could not be detected by the XRD measurements because of their low volume fraction. However with such a low fraction of unintended secondary phases remaining, the observed properties will be, although weakly shifted by the secondary phases, dominated by the main HMS phase and the trends observed can be clearly discussed as mainly originating from the HMS phase.

All materials (as-grown and annealed) presented in figure 3 were analysed by optical microscopy to search for the presence of MnSi. Some samples were also analysed by SEM-EDX to characterize the homogeneity of the dopant distribution in the HMS matrix and to identify secondary phases, if present. The microstructural changes of the 0.45%Al-HMS material are representative of that of the unstable materials (Re, Al, and Ge-doped), and therefore only the microstructure analysis of this material is reported here, as compared to that of the stable 4%V-HMS. A comparison of the optical microscopy features of the as-solidified and annealed materials is shown in figure 5. The MnSi phase is identified by different contrast to the bulk due to the effect of the MnSi etching step (this was confirmed by measuring a ratio [Si]:[Mn] = 1:1 using SEM-EDX). For both materials the presence of a small volume fraction of MnSi dendritic crystals at the surface contacting the mould is noticed. Because of the presence of a peritectic transformation it is expected that solidification starts first by MnSi nucleation at the mould surface and further by dendritic growth, and that later the HMS phase overgrows the MnSi dendrites in a melt slightly enriched in Si [43].

The main feature that distinguishes the as-solidified 4%V-HMS from the 0.45%Al-HMS material is the presence of MnSi layered precipitates in the latter, while these so-called striations are absent from 4%V-HMS. This observation confirms the general trend observed by other authors[33] on melt-grown V-doped HMS materials, although in contrast to them we did observe a minor amount of striations also in the 2%V-HMS. For the Al-doped material the striation defects are concentrated in the centres of the grains and often absent close to the grain boundaries. Local analysis of the composition by EDX showed that the concentration of Al dopant corresponds to about 0.2% substitution of Si in the striated regions and up to more than 1% substitution closer to the grain boundaries, while the nominal substitution amount is 0.45%. Similarly, we observe that for the Ge-doped materials, higher [Ge] closer to grain boundaries is correlated with the absence of striations there, as also reported by other authors for Ge-doped arc-melted samples[23]. As observed by Vives[23], above a critical Ge or

Al concentration MnSi striations do not precipitate during cooling after solidification. As will be discussed later, this is likely due to the stabilization effect of the substituted element on the $\gamma(T)$ characteristic above a critical concentration. In our case the concentration gradients originate from dopant segregation during RGS solidification. Note that the presence of gradients in the concentration of substitution elements imply that our materials are electrically inhomogeneous in the as-solidified state. These inhomogeneities appear at a scale smaller than that of the grain size (in the order of several hundred μm), thus they are much smaller than the sample size used for the measurement of the thermoelectric properties (or the size of thermoelectric element in devices). During the characterization of the thermoelectric stability the properties are therefore 'averaged out', no significant sample-to-sample variation can be noticed, and the measured properties are reliable with respect to the considered application.

The effect of annealing the samples in air at 600 °C for 10 hours is also shown in figure 5. We do not observe significant microstructural changes for the 4%V-HMS, whereas for all the other materials (including the 2%V-HMS), we observe a layer of MnSi at the grain boundaries, as revealed by the dark contrast in the optical microscopy images. Local SEM-EDX analysis confirmed that the stoichiometry of the grain boundary (GB) precipitates is approximately [Si]:[Mn] = 1:1. The morphology of the striation defects is also different after annealing: striations disappeared completely in some regions or broke down into discontinuous dotted lines. For the as-grown and annealed Al-doped materials, microcracks are often observed along the striations and for the annealed materials voids are present at the MnSi-rich grain boundaries (denoted as 'GB voids' in figure 5). Whether or not these voids are induced by the sample preparation procedure, in both cases we conclude that the interface between HMS and the MnSi phase is mechanically weak due to the significant lattice mismatch [28,29,31]. Finally it is worth mentioning that the striation defects have an orientation corresponding to a tilt of at most about 30˚ with the wafer plane. EBSD measurements confirmed a preferential orientation with the c-axis pointing out of wafer plane. This implies that any anisotropy in the thermoelectric properties, if present, should result in properties in plane different from cross plane. The 4%V-HMS material is the only one that does not show MnSi precipitation as striations or at grain boundaries in as-grown and annealed samples. This is also the only electrically stable material. We can thus correlate electrical stability with the absence of MnSi in this material. We are thus able to propose the following two hypotheses:

1 The formation of MnSi results in microcracks and lowers the charge carrier mobility.

2 The formation of MnSi is the result of structural changes (e.g, the γ ratio) in the HMS lattice, which also influences the charge carrier density via equations [1] and [2].

3.1.3 High temperature structural characterization and Hall measurements

To clarify hypotheses 1 and 2 we first investigated how the structural parameters of as-solidified 0.45%Al-HMS, 2%V-HMS and 4%V-HMS evolve between room temperature and 600 °C using HT- powder XRD on as-solidified materials. The samples are the same as for the measurements shown in figure 4. We chose the timescale of the HTXRD measurements and the exposure time at high temperature (total cycle time: 17 hours, time above 500 °C: 4.5 hours) to be a similar order of magnitude to the timescale over which changes in the electrical properties were measured (see figure 1). The complete set of unit cell parameters are plotted in the supplementary information (Figure S2). Figure 6 shows the evolution of γ as a function of temperature and measurement sequence. In essence, plotting $\gamma(T)$ is equivalent to characterizing the position of the HMS phase in the temperature-composition phase diagram. Figure 6 demonstrates that the HMS phase composition and structural parameters for 0.45%Al-HMS and 2%V-HMS change during the measurement: the HMS phase is enriched with Si upon heating above about 300 °C, primarily due to a negative expansion coefficient of the silicon sub-lattice in the c-direction during heating, i.e. the Si sub-cell contracts in the c-direction while the Mn subcell expands (see Figure S2, supplementary information). Upon cooling the expansion coefficient of both sub-lattices in the c-direction is similar, γ is stable and the HMS phase composition remains unchanged.

Kikuchi et al.[18] showed that the expansion coefficient of the Si sublattice in the c-direction is higher than that of the Mn sublattice in the temperature range 500-900 °C. This results in the HMS

phase becoming more Si-rich upon cooling (see Figure 6) and is in fact the driving force for the formation of MnSi striation precipitates during the cooling of melt-grown HMS crystals as observed by several authors[20,23,44]. We observe MnSi striation precipitates in our as-solidified 0.45%Al-HMS and 2%V-HMS materials, therefore we expect that the $\gamma(T)$ for these materials is similar in shape to that of Kikuchi et al.[18] above 600 °C. However, in our case these materials are likely not stabilized due to the fast cooling rate between the solidification temperature and room temperature in the RGS process (of the order of 2 °K/s). Thus, during synthesis the HMS phase relaxes only partially upon cooling and γ is kinetically 'locked' to values lower than the thermodynamically stable value. During the XRD measurement and the annealing tests, the HMS phase stabilizes to higher γ values. This explains the changes in MnSi striation morphology and the appearance of MnSi at grain boundaries (Figure 5) for the samples that had a similar exposure time at high temperature. In the 4%V-HMS material, the absence of MnSi striation precipitates suggests that the composition of the HMS phase solidified at high temperature is stable down to room temperature. This is supported by the temperature-independent $\gamma(T)$ characteristic. These measurements clearly show that stable HMS thermoelectric materials can be obtained by avoiding structural changes between the synthesis temperature and the temperature range of operation in a module. In other words the two sub-lattices should have the same expansion coefficient along the c axis and γ should be independent of temperature. The manipulation of $\gamma(T)$ can be achieved by adding optimized amounts of substitution elements[24,25], and we have shown that this approach can be used to stabilize the HMS phase over the room temperature-to-600 °C range using a sufficiently high amount of vanadium (hence the 2%V-HMS is unstable). One may further generalise to state that the use of substitution elements that shifts γ to sufficiently (lower) values close to that at the synthesis temperature helps to prevent the precipitation of MnSi striations. Thus 2%V-HMS is unstable because its γ value is too high (see $\gamma(T)$ during cooling in figure 6).Substitution of Si by Ge above a certain concentration was shown by several researchers to result in the same behaviour as observed here for V substitution (γ shifted to lower values and suppressed MnSi precipitates above a certain [Ge]) supporting this general statement. However in our case large [Ge] gradients most likely prevent sufficiently high substitution in the intra-grain regions such that MnSi still precipitates[23,24,31,32].

To examine the relations between changes in the structure and the electrical resistivity, considering as a first approximation a simple single band model, we compared the room temperature charge carrier density estimated by equations [1] and [2] with that measured by the Hall technique, before and after annealing. The results are summarized in figure 7, which compares the Hall carrier density measured at room temperature on as-solidified materials and on samples annealed for 10 hours at 600 °C in air with the carrier density estimated from the VEC model using the compositions determined from room temperature powder XRD data at the beginning and end of the measurement cycle (data from the samples in figure 6). In equation (1) we use the nominal substitution levels x and y with the assumption that the solubility limit is not exceeded, as confirmed by the absence of aluminium or vanadium silicides (XRD data, figure 4). Our Hall concentration data fits very well with that recently published by Miyazaki et al. for V-doped samples[25] and with that of Chen et al. for the Al-doped samples[5]. Figure 7 shows a good correlation between the measured change in carrier density and that predicted by the VEC model. This implies that the structural changes occurring during annealing result in a reduction of the charge carrier density by 20-30%, which is of the same order of magnitude as the decrease in electrical conductivity shown in figure 3. This means that the changes in structural parameters after high temperature exposure shown in figure 6 for 2%V-HMS and 0.45%Al-HMS directly correlate with a reduction of the charge carrier density. The charge carrier mobility was not significantly influenced by the annealing step, and microcrack formation and/or development are likely not responsible for the change in the electrical properties (hypothesis 1). The presence of MnSi precipitates is therefore not the root cause for the changes of electrical properties, instead the structural evolution at high temperature is the cause for both the formation of MnSi precipitates and changes of the electrical properties. Additionally if cracks would appear or develop during annealing one would not expect quantitatively reproducible measurements of the resistivity change. Instead, our measurements support hypothesis 2, i.e. the reduction of the electrical resistivity is the result of loss of charge carriers due to structural changes. Compared to the 4%V-HMS, the 2%V-HMS is not sufficiently substituted with V, its structural parameters are temperature-dependent and the carrier

concentration is reduced accordingly following equation 1 upon high temperature exposure.

As a final remark we note that in a rigid band picture the reduction in charge carrier density upon annealing will shift the electrochemical potential towards the gap and with that also the Seebeck coefficient is expected to significantly increase (see Appendix). However this is not the case in our measurements. This observation is consistent with the measurements of Chen et al., where Al doping increased the charge carrier density by up to 20% but the Seebeck coefficient was only weakly affected [5]. We take this as a clear hint on a change of the band structure close to the gap with changing carrier density. With increased V content we observe a better accordance of the transport properties to a model with higher effective mass which points to flatter bands and, with that a weaker change of the electrochemical potential with carrier density. Clearly, more research is needed to study the effects of the carrier concentration and of the crystal structure (γ value) on the band structure and occupancy close to the chemical potential and understand how these parameters influence the Seebeck coefficient of HMS materials.

3.2 Thermoelectric performance

We now focus on the thermoelectric performance of the HMS materials. Based on the results discussed in the previous section we chose to compare the thermoelectric properties of the materials after annealing for 10 hours at 600°C in air in order to reduce the effect of high temperature instabilities and compare the materials on a fairer basis. The low temperature Hall measurements and the high temperature thermoelectric properties are reported in figure 8. Note that the Hall data, the high temperature resistivity and Seebeck coefficient data reported in figure 8, and the electrical properties reported in figure 1 and figure 3 agree within measurement error even though different measurement setups were used. Despite our efforts to reduce the instabilities by pre-annealing, the electrical resistivity data between room temperature and 700°C clearly show that the electrical properties are not stabilized for all materials: the resistivity still increases during the measurement for Ge and Al-doped HMS. This is consistent with our observation that the resistivity still increases after 10 hours at 600 °C (figure 1 and figure 3) for these materials. However, the 3%Re-HMS show a resistivity *decrease* during the measurement: this contradicts our data in figure 1 and figure 3. The hysteresis behavior of the resistivity of this material could be related to a slow kinetics of γ change following the temperature-time profile of the measurement with a delay. If for 2%V-HMS $\gamma(T)$ behaves qualitatively as the undoped sample of Kikuchi et al.[18] above 600 °C (figure 6), delayed γ changes would result in a hysteresis in the carrier density (hence in the resistivity) consistent with the measurement. The 4%V-HMS is stable during the high temperature measurements, which is consistent with the stability study.

Figure 8 shows that the V-doped HMS samples have significantly different electrical properties to the Al, Ge and Re-doped materials. The higher hole concentration of 2%V and 4%V HMS compared to the other materials is the result of the stability of V in the structure, while the other materials seem to stabilize at a carrier concentration of about 1.64×10^{27} m^{-3} at 300 K (figure 8). Perhaps unexpected is the observation that the carrier concentration of the V-doped HMS materials increases with increasing temperature: unless very close to 0 K p-type thermoelectric materials typically possess a filled valence band and one does not expect this behaviour. This may be the result of impurity levels in the band gap. The Hall measurements also show a significantly lower charge carrier mobility for the V-doped materials, and a different temperature dependence. The Al, Ge and Re-doped materials all have the typical temperature dependence $\mu_L \propto T^{1.5}$ demonstrating that lattice-phonon scattering is the dominant limiting factor for carrier transport, as also concluded from measurements on undoped or lightly doped HMS materials by other authors[5,6]. The mobility of the V-doped materials is nearly an order of magnitude lower and varies with temperature as $\mu \propto T^{-0.5}$. Contrary to the Al, Ge and Re-doped materials for which the resistivity vanishes when the temperature tends to 0 K (confirming the phonon-limiting behaviour of the electrical transport), the resistivity of the V-doped materials remains significant at temperatures close to 0 K. Overall the temperature dependence of the Seebeck coefficient and of the electrical resistivity is significantly less strong for the V-doped materials. This is precisely the nearly temperature-independent resistivity that confers the superior figure of merit for the 4%V-HMS material. Finally we note that the charge carrier concentration and mobility of the Ge and V-doped samples have comparable value as that of arc-melted samples with similar substitution levels recently published by Miyazaki et al. [25]. The lower

mobility of V-doped HMS materials, their different temperature dependence and higher charge carrier density suggests that ionized impurity scattering is an additional limitation to the transport properties of these materials compared to the Al, Ge, and Re-doped materials. In general, the scattering time dominates the temperature dependence of the mobility ($\mu(T) \propto (e/m)\,\tau(T)$ where e and m are the electron charge and mass, respectively). The scattering time for ionized impurities scales as $\tau_i \propto T^{1.5}$, and that of phonons as $\tau_L \propto T^{-1.5}$. When both effects occur simultaneously the total scattering time τ will follow Matthiessen's rule as:

$$\frac{1}{\tau} = \frac{1}{\tau_L} + \frac{1}{\tau_i} \tag{3}$$

Equation (3) implies that in the case of mixed scattering the temperature exponent of τ varies between -1.5 and 1.5, which is the case for the V-doped samples. Based on these observations we choose to use the mixed scattering single parabolic band model of Fistul to describe the behaviour of the V-doped materials[45]. The mobility depends on both the scattering time for acoustic vibrations $\tau_L = \tau_{0L}\,\varepsilon^{-1/2}$ and the scattering time for ionized impurities $\tau_i = \tau_{0i}\,\varepsilon^{3/2}$ where ε is the reduced carrier energy. Using equation (3) the total scattering time can be written as $\tau = \tau_{oL}\,\varepsilon^{3/2}/(\varepsilon^2 + a^2)$, where the scattering index $a = \sqrt{\tau_{oL}/\tau_{oi}}$ is a measure of the strength of ionized impurity scattering relative to acoustic phonon scattering. In this framework the electrical properties can be written as follows:

$$\sigma(\eta, a) = \frac{8\pi\, m^{*\frac{1}{2}} e^2}{3h^3} (2k_B T)^{\frac{3}{2}}\, \tau_{0,L}\, \Phi_3(\eta, a) \tag{4}$$

$$S(\eta, a) = \frac{k_B}{e}\left[\frac{\Phi_4(\eta, a)}{\Phi_3(\eta, a)} - \eta\right] \tag{5}$$

$$[p] = 4\pi\left(\frac{2m^* k_B T}{h^2}\right)^{\frac{3}{2}} F_{\frac{1}{2}}(\eta) \tag{6}$$

$$\mu = \frac{2e}{3m^*}\tau_{0,L}\,\frac{\Phi_3(\eta, a)}{F_{\frac{1}{2}}(\eta)} \tag{7}$$

$$\Phi_n(\eta, a) = \int_0^\infty \frac{\varepsilon^n \exp(\varepsilon - \eta)}{(\varepsilon^2 + a^2)[1 + \exp(\varepsilon - \eta)]^2}\, d\varepsilon \tag{8}$$

Here $F_{1/2}(\eta)$ is the Fermi integral of order ½. η, m^*, k_B, h are the reduced Fermi energy, the density of states effective mass, Boltzmann coefficient and Planck constant respectively. It is assumed that the density of states effective mass is equal to the mobility effective mass. This model is an extension of the more commonly used single parabolic band model where only acoustic phonon scattering is considered[46] (limiting case $a = 0$). This mixed scattering model has also been used by several authors to describe the superior properties of highly substituted skutterudites[47,48]. We solved the set of equations [4]-[7] numerically for two sets of $\{m^* ; a\}$ to illustrate the differences between the 4%V-HMS and the Re, Ge and Al substituted materials. We assumed that $[p]$ is temperature-independent and chose the value measured at room temperature to estimate $\eta(T)$ (equation (6)). First, we fit the model to the data of the Re, Ge and Al-doped samples using $a = 0$ ($\tau_i \to \infty$ negligible ionized impurity scattering) and $[p] = 1.64 \times 10^{27}$ m^{-3} (as measured at room temperature). Using the Seebeck coefficient data and equation [5] we obtain $m^* = 7.5\, m_0$ from equation (6), a value similar to that previously published[5]. τ_{oL} is estimated by fitting the mobility data, resulting in $\tau = \tau_{oL} = 19.2$ fs at room temperature. The same value of τ_{oL} is used for V-doped samples since there is *a priori* no reason that phonon scattering affects the electrical transport properties differently for V-doped samples and Al, Ge and Re-doped materials. However, to reproduce the specific features of the data of V-doped HMS it is necessary to introduce ionized impurity scattering (i.e. $a > 0$). Using $m^* = 10.5\, m_0$ and a (300K) = 4.3 (τ_i(300K) = 1 fs), the model reproduces the room temperature data of 4%V-HMS well. Figure 8 shows that the essential differences between the V-doped samples and the Al, Ge and Re-doped samples are well described by introducing ionized impurity scattering. Especially the significant differences in the temperature dependence of the mobility, the low temperature resistivity data and the high temperature Seebeck coefficient data (at temperatures below about 450°C) are well reproduced: the mobility scales as $\mu \propto T^{-0.5}$, the resistivity does not vanish towards 0 K, and the temperature dependence of $S(T)$ is less pronounced. However, while the model qualitatively predicts that the resistivity of V-doped materials becomes lower than that of the other samples at high temperature, there is a significant discrepancy between the values predicted by the model and the

measurements.

The thermal conductivity of 4%V-HMS is significantly lower than that of the other samples. Since this material also has a lower electrical resistivity, the electrical contribution to the thermal conductivity should be higher: this means that the lattice contribution to the thermal conductivity overcompensates the higher electrical contribution. Although this effect should be studied in more detail, we hypothesize that this may be the result of an alloy scattering effect. Overall, the significantly higher ZT of 4%V-HMS is the result of the improved power factor and lower thermal conductivity. ZT_{max}=0.52 is estimated for this material. Most importantly, this material is also stable at high temperature, in contrast to the Al, Ge, Re-doped samples and the 2%V-HMS material.

4 Conclusions

On the basis that the performance of thermoelectric materials should remain stable under relevant device temperature conditions, we have used several procedures to measure the structural and thermoelectric stability of HMS materials substituted with different elements. We demonstrate that most HMS materials prepared by the RGS technique have a temperature-dependent γ factor and are structurally and electrically unstable at 600°C. Specifically, structural changes result in the formation of MnSi precipitates and reduction of the charge carrier concentration of a magnitude comparable with the electrical conductivity decrease. Therefore we conclude that the structural changes are responsible for the unstability. By substituting 4% of Mn by V the γ factor then becomes temperature independent in the range of interest, resulting in the prevention of MnSi precipitate formation and stable electrical properties when exposed to 600°C for up to 45 h. As a topic for future research, it would be interesting to confirm the structural stability of this material up to the melting point.

The 4%V-HMS material also exhibits the highest ZT. This is in part due to its thermal stability, but also because ionized impurity scattering effects mitigate the reduction of the Seebeck coefficient due to the higher charge carrier concentration. In combination with a lowered thermal conductivity, the estimated ZT of this material reaches state-of-the-art values.

Appendix

For example, taking the Hall carrier concentration data for 0.45%Al-HMS (figure 7) and using the single parabolic band model at 300K (equations (4)-(8) with $a = 0$, $m^* = 7.5\ m_0$), one finds that the carrier concentration change during the 10 h annealing step corresponds to a decrease in electrical conductivity from 90×10^4 S/m to 70×10^4 S/m (-22% - note that the absolute values fit the data of figure 3 fairly well) and to an increase of the Seebeck coefficient from 83μV/K to 101μV/K (+22%, whereas measurements show a change from 110 μV/K to 100μV/K, i.e. -9%).

References

[1]   I. Cohen, M. Kaller, G. Komisarchik, D. Fuks, Y. Gelbstein, Enhancement of the thermoelectric properties of n-type PbTe by Na and Cl co-doping, J. Mater. Chem. C. 3 (2015) 9559–9564. https://doi.org/10.1039/C5TC01781E.

[2]   G. Komisarchik, D. Fuks, Y. Gelbstein, High thermoelectric potential of n -type Pb 1− x Ti x Te alloys, J. Appl. Phys. 120 (2016) 055104. https://doi.org/10.1063/1.4960573.

[3]   G.M. Guttmann, D. Dadon, Y. Gelbstein, Electronic tuning of the transport properties of off-stoichiometric Pb x Sn 1− x Te thermoelectric alloys by Bi 2 Te 3 doping, J. Appl. Phys. 118 (2015) 065102. https://doi.org/10.1063/1.4928459.

[4]   O. Appel, Y. Gelbstein, A Comparison Between the Effects of Sb and Bi Doping on the Thermoelectric Properties of the Ti0.3Zr0.35Hf0.35NiSn Half-Heusler Alloy, J. Electron. Mater. 43 (2014) 1976–1982. https://doi.org/10.1007/s11664-013-2930-3.

[5]   X. Chen, A. Weathers, D. Salta, L. Zhang, J. Zhou, J.B. Goodenough, L. Shi, Effects of (Al,Ge) double doping on the thermoelectric properties of higher manganese silicides, J. Appl. Phys. 114 (2013) 173705. https://doi.org/10.1063/1.4828731.

[6]   M. Fedorov, V. Zaitsev, Thermoelectrics of Transition Metal Silicides, in: Thermoelectr. Handb., CRC Press, 2005: pp. 31-1-31–20. https://doi.org/10.1201/9781420038903.ch31.

[7]   T. Zhu, Y. Liu, C. Fu, J.P. Heremans, J.G. Snyder, X. Zhao, Compromise and Synergy in High-Efficiency Thermoelectric Materials, Adv. Mater. 29 (2017) 1605884. https://doi.org/10.1002/adma.201605884.

[8]   Y. Sadia, Z. Aminov, D. Mogilyansky, Y. Gelbstein, Texture anisotropy of higher manganese silicide following arc-melting and hot-pressing, Intermetallics. 68 (2016) 71–77. https://doi.org/10.1016/j.intermet.2015.08.009.

[9]   J. de Boor, T. Dasgupta, U. Saparamadu, E. Müller, Z.F. Ren, Recent progress in p-type thermoelectric magnesium silicide based solid solutions, Mater. Today Energy. 4 (2017) 105–121. https://doi.org/10.1016/j.mtener.2017.04.002.

[10]   G. Skomedal, L. Holmgren, H. Middleton, I.S. Eremin, G.N. Isachenko, M. Jaegle, K. Tarantik, N. Vlachos, M. Manoli, T. Kyratsi, D. Berthebaud, N.Y. Dao Truong, F. Gascoin, Design, assembly and characterization of silicide-based thermoelectric modules, Energy Convers. Manag. 110 (2016) 13–21. https://doi.org/10.1016/j.enconman.2015.11.068.

[11]   A. Yamamoto, S. Ghodke, H. Miyazaki, M. Inukai, Y. Nishino, M. Matsunami, T. Takeuchi, Thermoelectric properties of supersaturated Re solid solution of higher manganese silicides, Jpn. J. Appl. Phys. 55 (2016) 020301. https://doi.org/10.7567/JJAP.55.020301.

[12]   S.C. Ghodke, Effect of grain boundaries and partial substitution of transition metals on thermoelectric properties of higher manganese silicide, PhD thesis, Nagoya University, 2016.

[13]   S. Ghodke, N. Hiroishi, A. Yamamoto, H. Ikuta, M. Matsunami, T. Takeuchi, Enhanced Thermoelectric Properties of W- and Fe-Substituted MnSiγ, J. Electron. Mater. 45 (2016) 5279–5284. https://doi.org/10.1007/s11664-016-4688-x.

[14]   Y. Miyazaki, Superspace Group Approach to the Crystal Structure of Thermoelectric Higher Manganese Silicides MnSiγ, in: Neutron Diffr., 2012: pp. 231–242. https://doi.org/10.5772/36666.

[15]   L. Akselrud, R. Cardoso Gil, M. Wagner-Reetz, Y. Grin, Disorder in the composite crystal structure of the manganese "disilicide" MnSi1.73 from powder X-ray diffraction data, Acta Crystallogr. Sect. B Struct. Sci. Cryst. Eng. Mater. 71 (2015) 707–712. https://doi.org/10.1107/S2052520615019757.

[16]   D.C. Fredrickson, S. Lee, R. Hoffmann, The Nowotny chimney ladder phases: Whence the 14 electron rule?, Inorg. Chem. 43 (2004) 6159–6167. https://doi.org/10.1021/ic049897h.

[17]   D.C. Fredrickson, S. Lee, R. Hoffmann, J. Lin, The Nowotny chimney ladder phases: Following the cpseudo clue toward an explanation of the 14 electron rule, Inorg. Chem. 43 (2004) 6151–6158. https://doi.org/10.1021/ic049427n.

[18]   Y. Kikuchi, T. Nakajo, K. Hayashi, Y. Miyazaki, High temperature X-ray diffraction study on

incommensurate composite crystal MnSi – (3+1)-dimensional superspace approach, J. Alloys Compd. 616 (2014) 263–267. https://doi.org/10.1016/j.jallcom.2014.07.106.

[19]   Y. Miyazaki, D. Igarashi, K. Hayashi, T. Kajitani, K. Yubuta, Modulated crystal structure of chimney-ladder higher manganese silicides MnSiγ (γ∼1.74), Phys. Rev. B - Condens. Matter Mater. Phys. 78 (2008) 1–8. https://doi.org/10.1103/PhysRevB.78.214104.

[20]   I. Kawasumi, M. Sakata, I. Nishida, K. Masumoto, Crystal growth of manganese silicide, MnSi∼1.73 and semiconducting properties of Mn15Si26, J. Mater. Sci. 16 (1981) 355–366. https://doi.org/10.1007/BF00738624.

[21]   R. De Ridder, S. Amelinckx, The structure of defect manganese silicides, Mater. Res. Bull. 6 (1971) 1223–1234. https://doi.org/10.1016/0025-5408(71)90058-4.

[22]   H.Q. Ye, S. Amelinckx, High-resolution electron microscopic study of manganese silicides MnSi2−x, J. Solid State Chem. 61 (1986) 8–39. https://doi.org/10.1016/0022-4596(86)90003-4.

[23]   S. Vivès, Microstructure control and transport properties of incommensurate manganese silicide based alloys for thermoelectricity, PhD thesis, Universite de Bordeaux, 2015.

[24]   D.Y.N. Truong, Thermoelectric Properties of Higher Manganese Silicides, PhD thesis, University of Waterloo, Waterloo, Ontario, Canada, 2015.

[25]   H. Hamada, Y. Kikuchi, K. Hayashi, Y. Miyazaki, Crystal Structure and Thermoelectric Properties of the Incommensurate Chimney–Ladder Compound VGeγ (γ ∼1.82), J. Electron. Mater. 45 (2016) 1365–1368. https://doi.org/10.1007/s11664-015-4036-6.

[26]   A. Allam, P. Boulet, C. a. Nunes, J. Sopousek, P. Broz, M.C. Record, Phase transformations in Higher Manganese Silicides, J. Alloys Compd. 551 (2013) 30–36. https://doi.org/10.1016/j.jallcom.2012.10.016.

[27]   I. Aoyama, M.I. Fedorov, V.K. Zaitsev, F.Y. Solomkin, I.S. Eremin, A.Y. Samunin, M. Mukoujima, S. Sano, T. Tsuji, Effects of Ge Doping on Micromorphology of MnSi in MnSi ∼1.7 and on Their Thermoelectric Transport Properties, Jpn. J. Appl. Phys. 44 (2005) 8562–8570. https://doi.org/10.1143/JJAP.44.8562.

[28]   E.I. Suvorova, V. V. Klechkovskaya, Precipitates of MnSi cubic phase in tetragonal Mn4Si7 crystal, Crystallogr. Reports. 58 (2013) 854–861. https://doi.org/10.1134/S1063774513060229.

[29]   A.S. Orekhov, E.I. Suvorova, Study of doped higher manganese silicides crystals by transmission electron diffraction and electron backscatter diffraction, Crystallogr. Reports. 59 (2014) 78–87. https://doi.org/10.1134/S106377451401009X.

[30]   S.N. Girard, X. Chen, F. Meng, A. Pokhrel, J. Zhou, L. Shi, S. Jin, Thermoelectric Properties of Undoped High Purity Higher Manganese Silicides Grown by Chemical Vapor Transport, Chem. Mater. 26 (2014) 5097–5104. https://doi.org/10.1021/cm5023823.

[31]   L.D. Ivanova, A.A. Baikov, Higher Manganese Silicide Based Materials, J. Thermoelectr. 3 (2009) 60–66.

[32]   A.J. Zhou, X.B. Zhao, T.J. Zhu, S.H. Yang, T. Dasgupta, C. Stiewe, R. Hassdorf, E. Mueller, Microstructure and thermoelectric properties of SiGe-added higher manganese silicides, Mater. Chem. Phys. 124 (2010) 1001–1005. https://doi.org/10.1016/j.matchemphys.2010.08.017.

[33]   Y. Miyazaki, H. Hamada, K. Hayashi, K. Yubuta, Crystal Structure and Thermoelectric Properties of Lightly Vanadium-Substituted Higher Manganese Silicides (Mn1−xVx)Siγ), J. Electron. Mater. 46 (2017) 2705–2709. https://doi.org/10.1007/s11664-016-4937-z.

[34]   Y. Miyazaki, H. Hamada, H. Nagai, K. Hayashi, Crystal structure and thermoelectric properties of lightly substituted higher manganese silicides, Materials (Basel). 11 (2018) 926.

https://doi.org/10.3390/ma11060926.

[35] M. Apel, D. Franke, I. Steinbach, Simulation of the crystallisation of silicon ribbons on substrate, in: Sol. Energy Mater. Sol. Cells, 2002: pp. 201–208. https://doi.org/10.1016/S0927-0248(01)00165-9.

[36] G. Hahn, A. Schönecker, New crystalline silicon ribbon materials for photovoltaics, J. Phys. Condens. Matter. 16 (2004) R1615–R1648. https://doi.org/10.1088/0953-8984/16/50/R03.

[37] V. Petříček, V. Eigner, M. Dušek, A. Čejchan, Discontinuous modulation functions and their application for analysis of modulated structures with the computing system JANA2006, Zeitschrift Für Krist. - Cryst. Mater. 231 (2016). https://doi.org/10.1515/zkri-2015-1913.

[38] J. de Boor, C. Stiewe, P. Ziolkowski, T. Dasgupta, G. Karpinski, E. Lenz, F. Edler, E. Mueller, High-Temperature Measurement of Seebeck Coefficient and Electrical Conductivity, J. Electron. Mater. 42 (2013) 1711–1718. https://doi.org/10.1007/s11664-012-2404-z.

[39] J. de Boor, E. Müller, Data analysis for Seebeck coefficient measurements, Rev. Sci. Instrum. 84 (2013) 065102. https://doi.org/10.1063/1.4807697.

[40] Y. Miyazaki, Y. Saito, K. Hayashi, K. Yubuta, T. Kajitani, Preparation and Thermoelectric Properties of a Chimney-Ladder (Mn 1- x Fe x)Si γ (γ∼1.7) Solid Solution, Jpn. J. Appl. Phys. 50 (2011) 035804. https://doi.org/10.1143/JJAP.50.035804.

[41] N. Krendelsberger, F. Weitzer, J.C. Schuster, On the constitution of the system Al-Mn-Si, Metall. Mater. Trans. A. 33 (2002) 3311–3319. https://doi.org/10.1007/s11661-002-0319-7.

[42] A. Yamamoto, H. Miyazaki, M. Inukai, Y. Nishino, T. Takeuchi, Thermoelectric properties of Al–Mn–Si C40 phase containing small amount of W or Ta, Jpn. J. Appl. Phys. 54 (2015) 071801. https://doi.org/10.7567/JJAP.54.071801.

[43] H.W. Kerr, W. Kurz, Solidification of peritectic alloys, Int. Mater. Rev. 41 (1996) 129–164. https://doi.org/10.1179/095066096790151231.

[44] T. Kojima, I. Nishida, T. Sakata, Crystal growth of Mn15Si26, J. Cryst. Growth. 47 (1979) 589–592. https://doi.org/10.1016/0022-0248(79)90144-1.

[45] V.I. Fistul, Heavily Doped Semiconductors, Plenum, New York, 1969.

[46] A.F. May;, G.J. Snyder, Introduction to Modeling Thermoelectric Transport at High Temperatures, in: D.M. Rowe (Ed.), Mater. Prep. , Charact. Thermoelectr., CRC Press, 2012.

[47] S. Wang, J. Yang, L. Wu, P. Wei, W. Zhang, J. Yang, On Intensifying Carrier Impurity Scattering to Enhance Thermoelectric Performance in Cr-Doped Ce y Co 4 Sb 12, Adv. Funct. Mater. 25 (2015) 6660–6670. https://doi.org/10.1002/adfm.201502782.

[48] J.S. Dyck, W. Chen, C. Uher, L. Chen, X. Tang, T. Hirai, Thermoelectric properties of the n - type filled skutterudite Ba0.3Co4Sb12 doped with Ni, J. Appl. Phys. 91 (2002) 3698–3705. https://doi.org/10.1063/1.1450036.
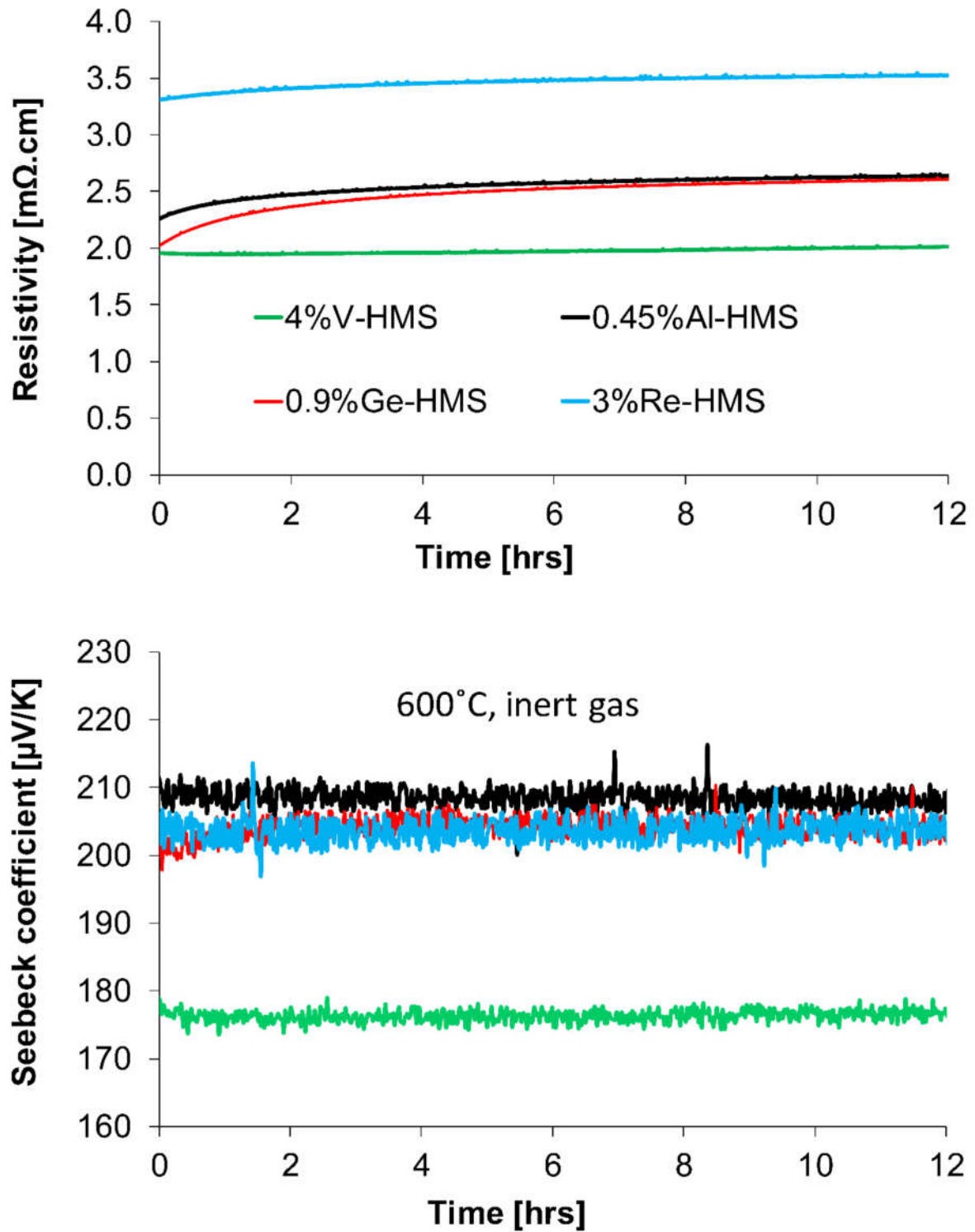
Figures and captions

Figure 1. (Color Online) Seebeck coefficient and electrical resistivity as a function of time at high temperature (600 ˚C) in inert gas (measurements Uni Groningen). The samples were as-solidified prior to the measurement.
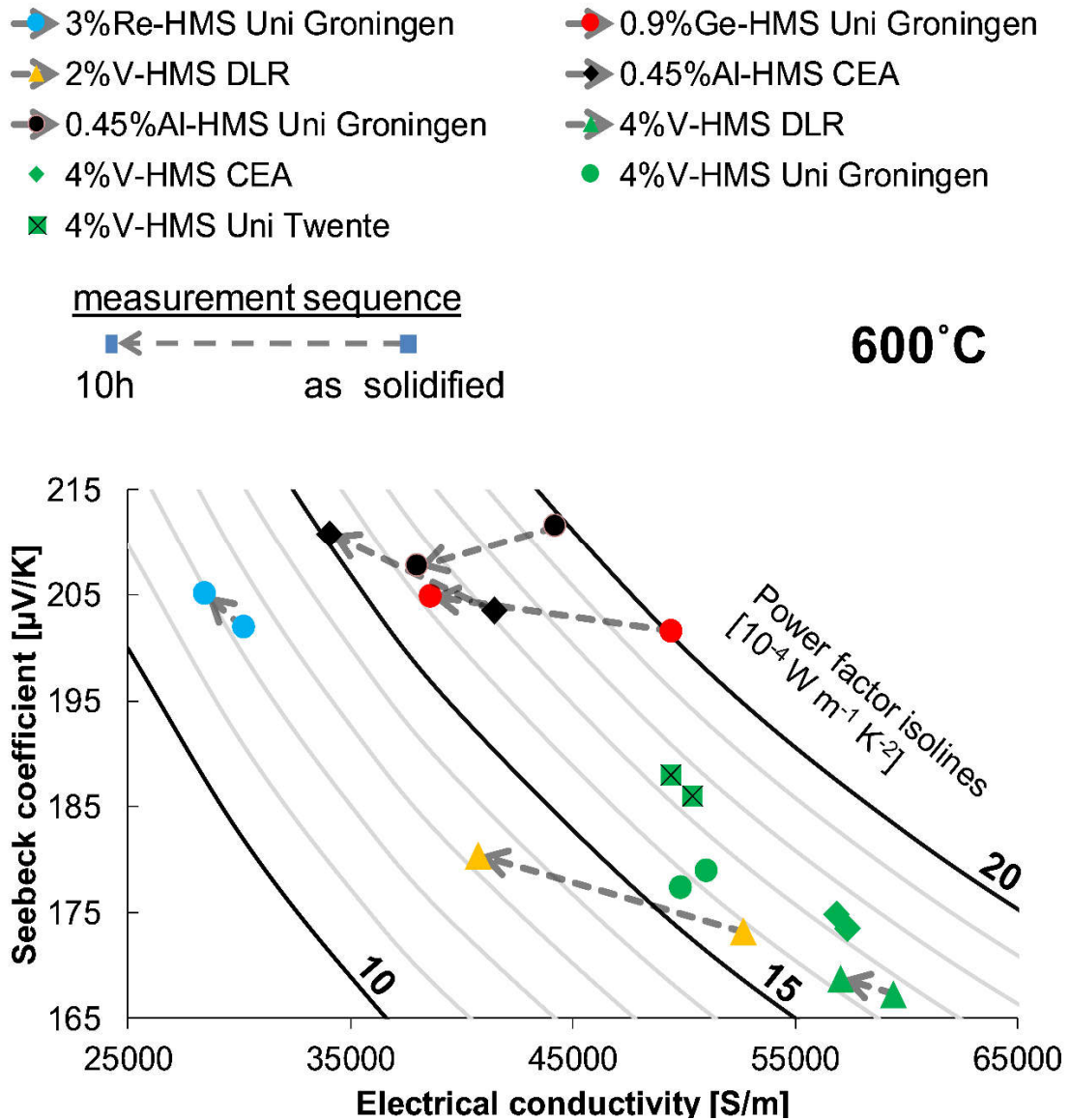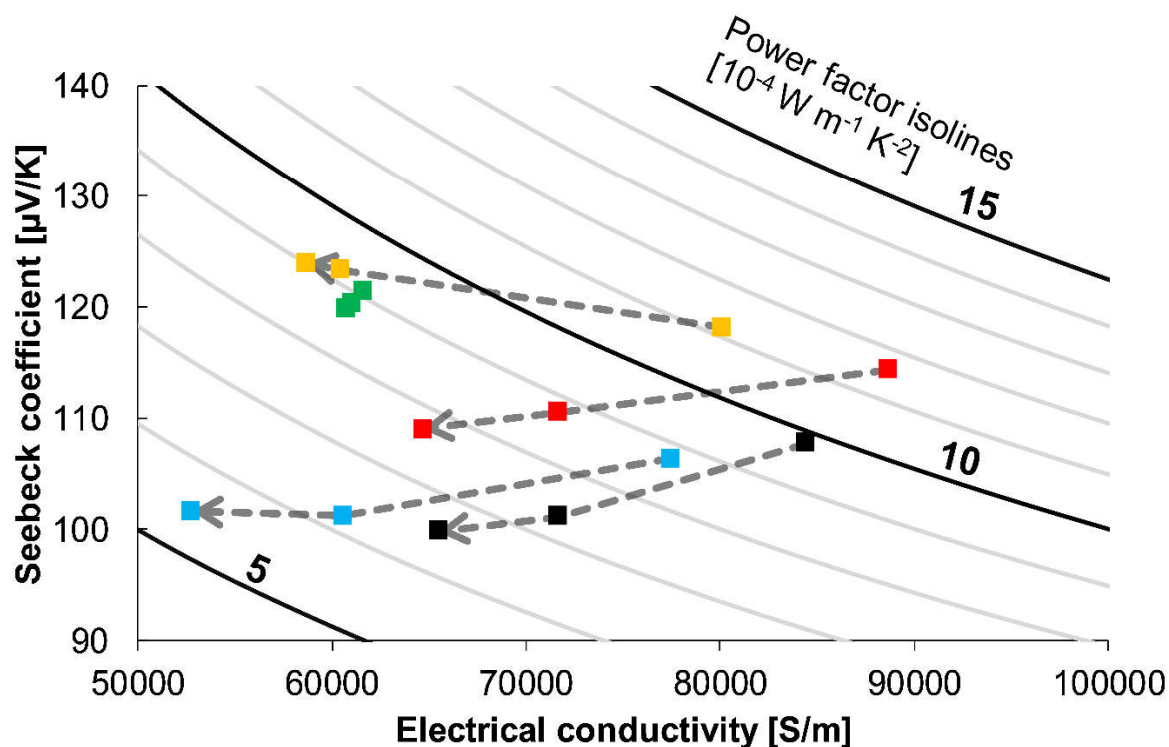
Figure 2. (Color Online) Seebeck coefficient and electrical conductivity of as-grown materials (points at start of arrows) and materials after 10 h annealing at 600°C (points at end of arrows). The curved lines are power factor isolines. Uni Groningen data are taken from Figure 1, CEA and Uni Twente data are taken from Supplementary information – Figure S1. DLR data (after 10 h) are taken from figure 8 (average between temperature ramp up and ramp down).

Figure 3. (Color Online) Seebeck coefficient and electrical conductivity of as-grown materials (points at start of arrows) and materials annealed for 10 h (second points along arrows) and 100 h (points at ends of arrows) in air at 600°C. The curved lines are power factor isolines. Each data point corresponds to the average of 3 to 5 replicated measurements. The 3 measurement points for 4%V-HMS overlap within the measurement error.
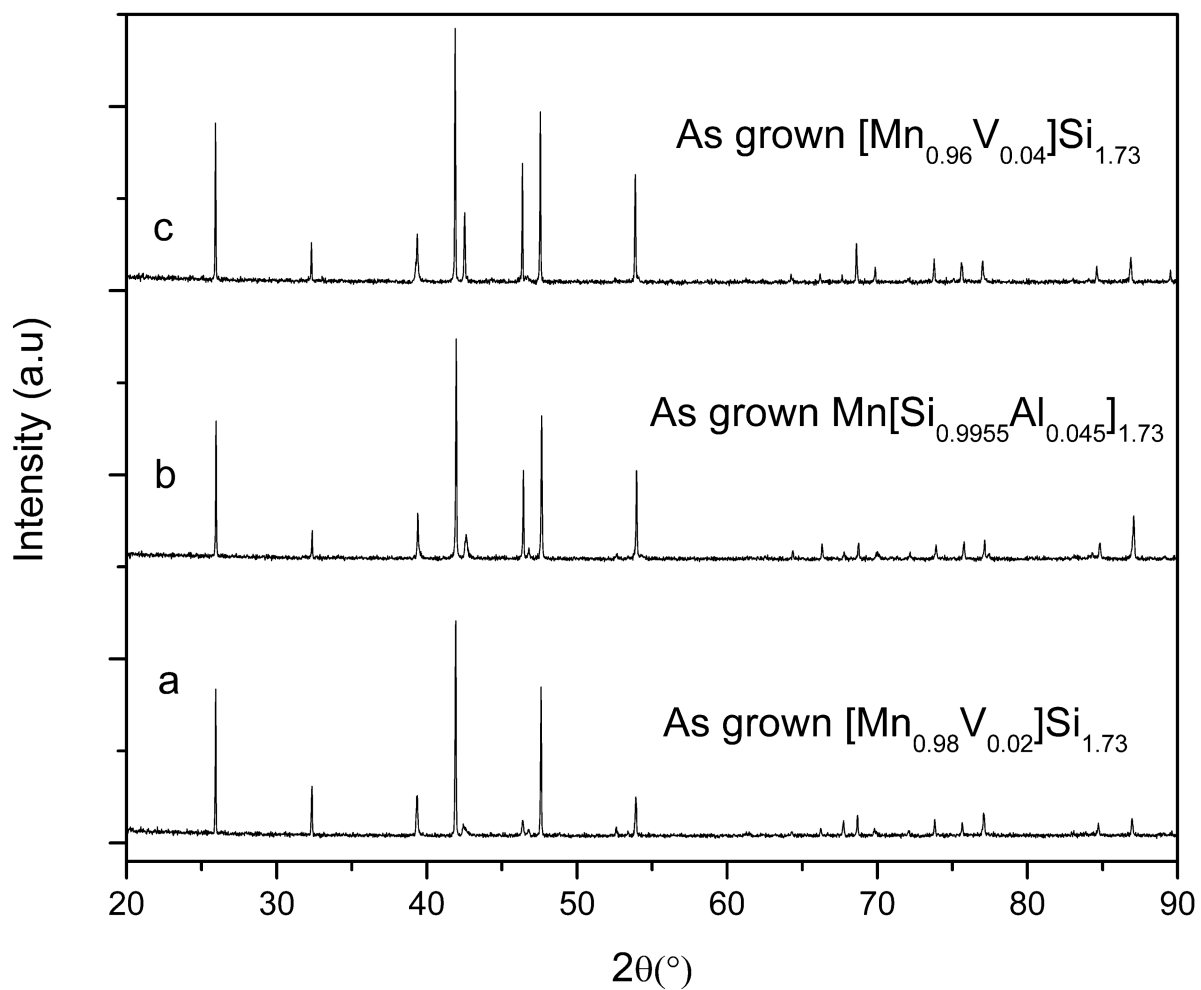
Figure 4. Room temperature XRD measurements of as-solidified (a) 2%V-HMS, (b) 0.45%Al-HMS, and (c) 4%V-HMS.
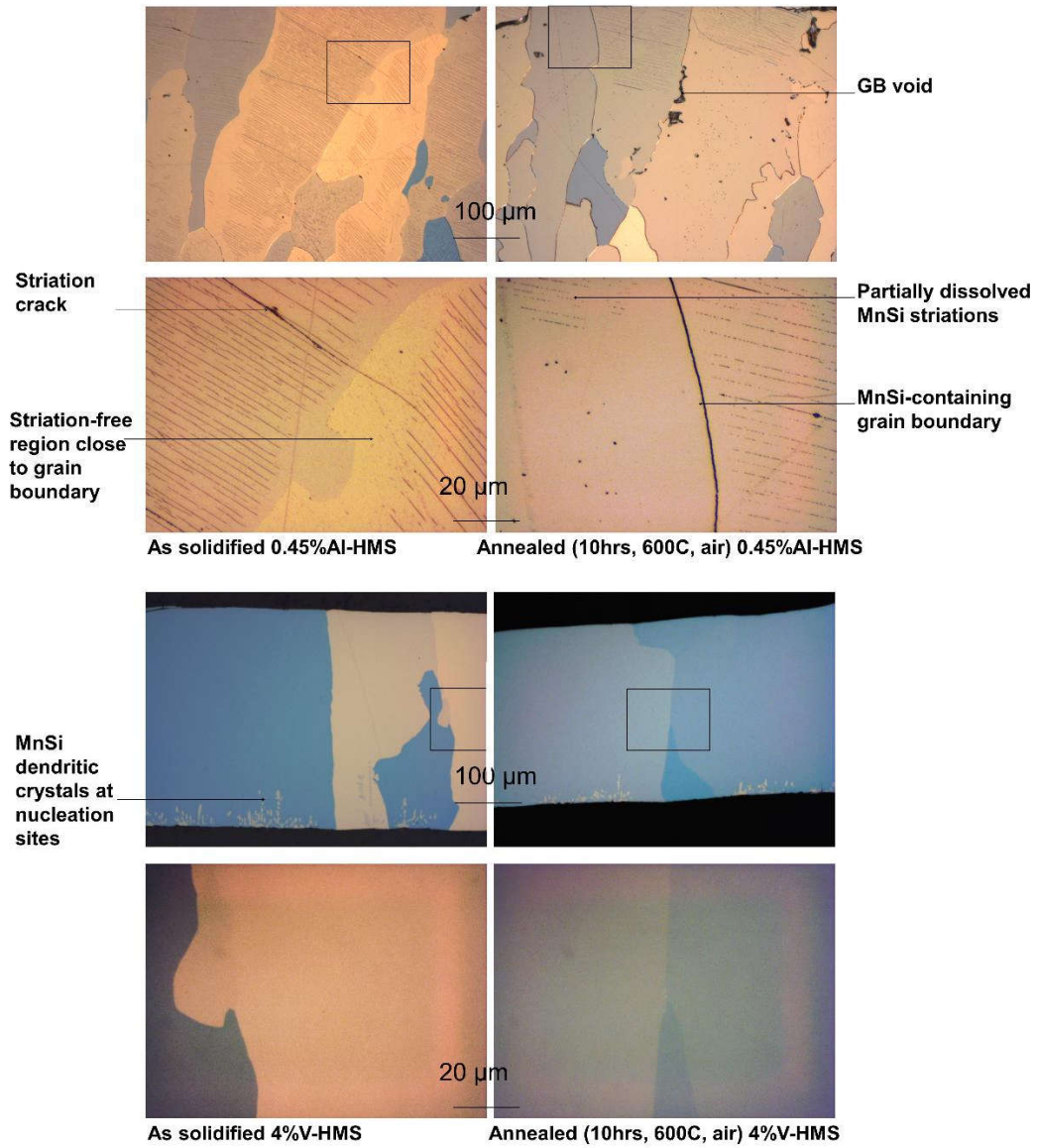
Figure 5. (Color Online) Optical microscopy images of polished cross sections of 0.45%Al-HMS (upper set) and 4%V-HMS (lower set). The solidification direction is from bottom to top on all images. Pictures are taken under polarized light at low magnification (top) and high magnification (bottom – regions corresponding to the black inset frames above). As-solidified samples are shown on the left and annealed samples (10 h at 600 °C in air) on the right. All cross sections were submitted to a MnSi etch to reveal the presence of the MnSi phase.
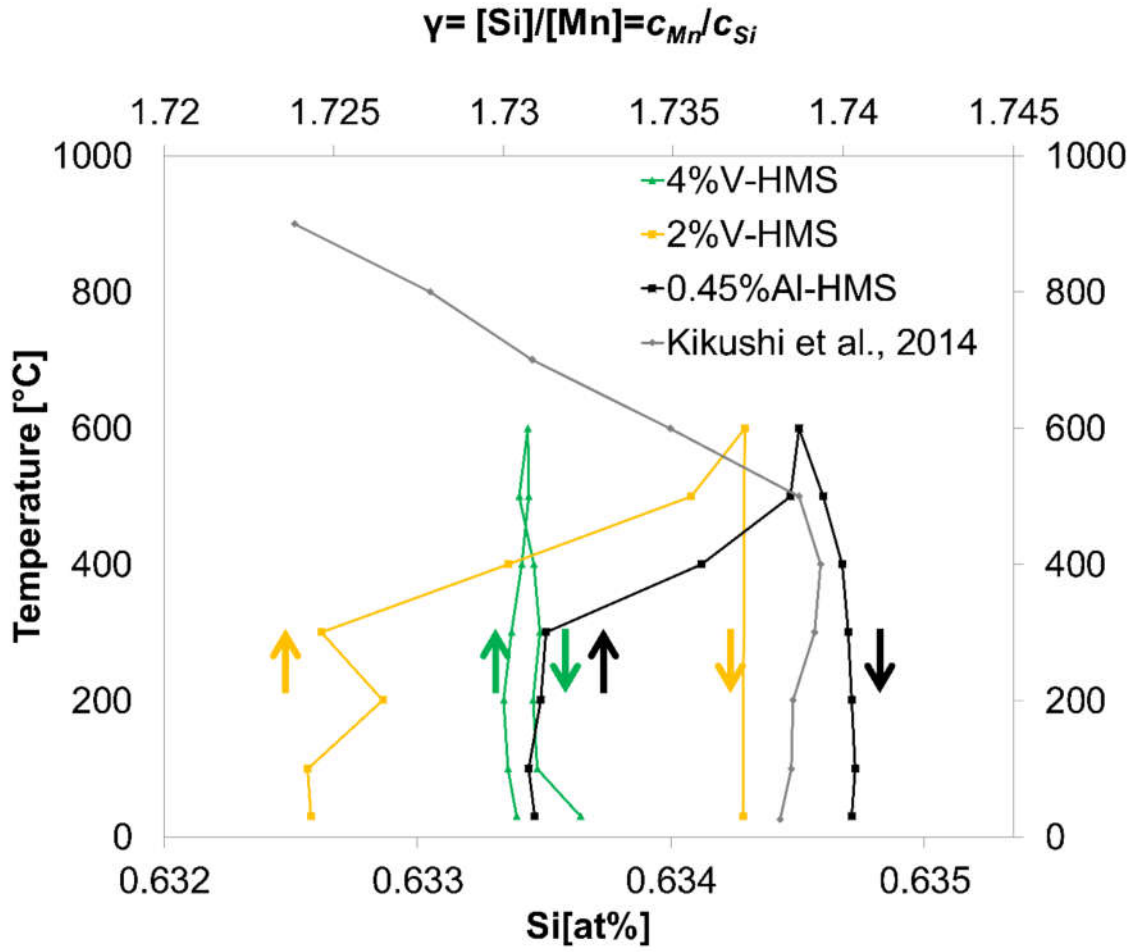
Figure 6. (Color Online) $\gamma(T)$ structural parameter for as-solidified HMS materials measured by HTXRD. The arrows show the evolution of γ upon heating (↑) and cooling(↓). The data of Kikuchi et al.[18] for undoped HMS prepared by arc melting is shown for comparison and discussion purposes.
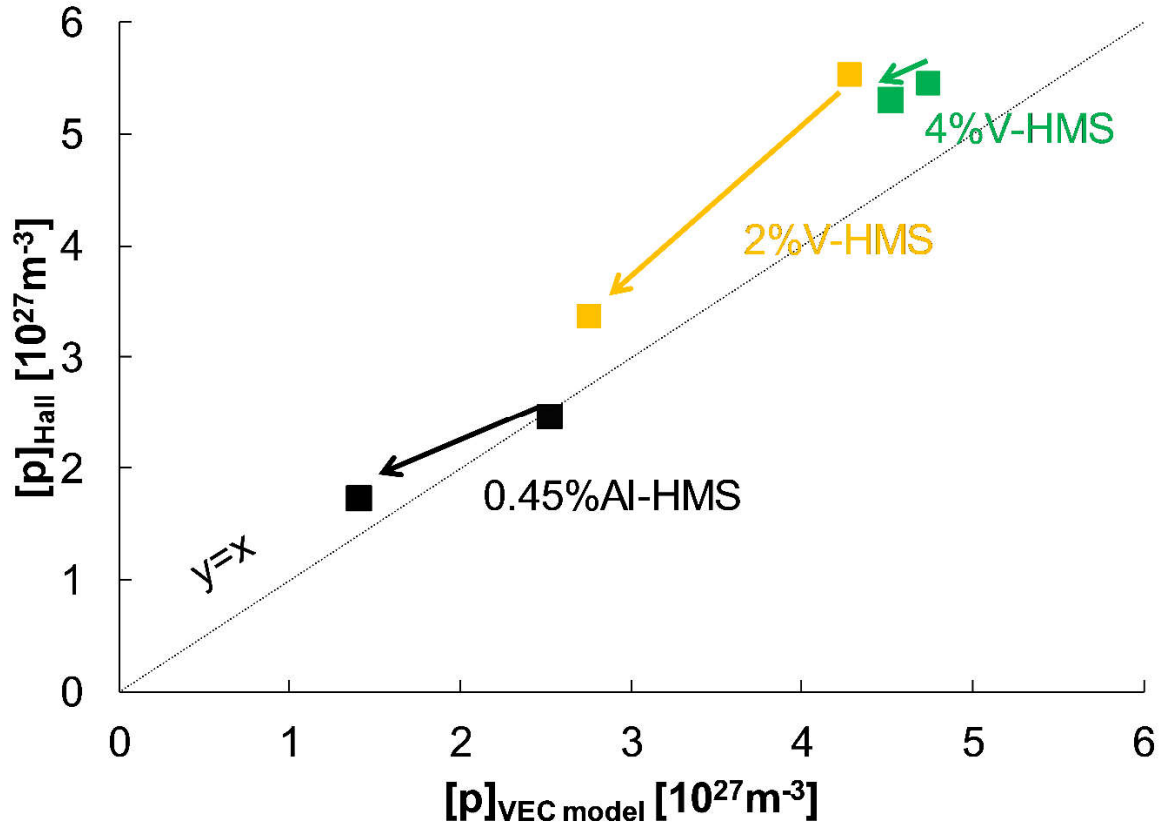
Figure 7. (Color Online) Effect of annealing on the charge carrier density of 0.45%Al-HMS, 2%V-HMS, and 4%V-HMS. Hall measurements (vertical axis) are compared to the carrier density estimated from the VEC model (horizontal axis). The straight line corresponds to y=x.
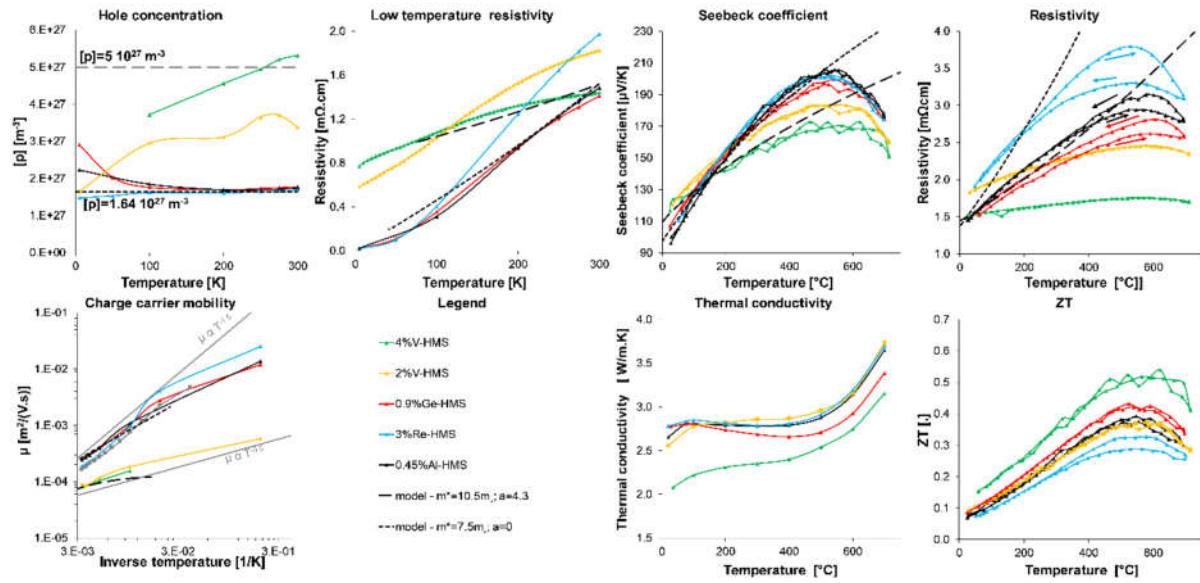
Figure 8. (Color Online) Low temperature (left) and high temperature (right) thermoelectric properties of HMS materials produced by the RGS process containing different substitution elements. All materials were annealed for 10 hours at 600 °C in air prior to the measurements. Materials doped with Ge, Al and Re have not reached a stable state after this thermal treatment. The coloured arrows in the high temperature resistivity plots show the data acquisition sequence during heating and cooling. Dashed black lines are model results for different effective masses m^* and scattering parameters a at 300 K.